Journal of Oceanography (2021) 77:173–184
https://doi.org/10.1007/s10872-020-00584-0

SPECIAL SECTION: ORIGINAL ARTICLE

Ocean Mixing Processes (OMIX): Impact on Biogeochemistry, Climate and Ecosystem

Role of tide-induced vertical mixing in the deep Pacific Ocean circulation

Takao Kawasaki[1] · H. Hasumi[1] · Y. Tanaka[2]

Received: 28 July 2020 / Revised: 30 November 2020 / Accepted: 6 December 2020 / Published online: 12 January 2021

Abstract
We investigate the control mechanisms of the deep Pacific Ocean circulation by introducing updated methods for parameterizing tidal mixing. The column-integrated rates of dissipation in near- and far-fields are derived from the tidal energy conversion and dissipation rates estimated by a high resolution tide model. In the calculation of the far-field mixing, its dependency on stratification is taken into account based on theoretical and observational knowledge. Unlike previous studies that did not take the stratification dependence into account, the far-field mixing does not function to significantly enhance the deep Pacific Ocean circulation. The deep Pacific Ocean circulation is also found to be insensitive to the decay scale height of the near-field mixing. However, these factors affect the reproducibility of the radiocarbon distribution, especially its minimum in the upper deep layer, through their influence on the mixing with the shallower layers.

Keywords Tide-induced vertical mixing · Deep pacific ocean circulation · Ocean modeling

1 Introduction

The Pacific Ocean is the largest basin in the world ocean and is thought to be the principal low-latitude upwelling region in the global thermohaline circulation (Schmitz 1995; Talley 2013). Owing to a lack of deep water formation in the Pacific Ocean, the water characteristics are more uniform in the deep Pacific Ocean than in the deep Atlantic Ocean. Consequently, observational description of the deep Pacific Ocean circulation is falling behind the other basins (Lumpkin and Speer 2007; Talley 2013).

The lower part of Circumpolar Deep Water (CDW) is transported northward in the Pacific lower deep layer (deeper than ~ 3500 m) (Roemmich et al. 1996; Rudnick 1997). Mooring observations estimated the volume transport through several deep passages in the Pacific Ocean. At the Samoan Passage (~ 10°S) connecting the South and Central Pacific Basins, the mooring observation in 1992–94 demonstrated that the total volume transport of the deep water is 6.0 ± 0.5 Sv (1 Sv = 10^6 m^3 s^{-1}; Rudnick 1997). Other small northward flows were also observed in the vicinity of the Samoan Passage (Roemmich et al. 1996), and the total northward transport of deep water at 10°S was estimated to be 10.6 ± 1.7 Sv. The mooring observation at the Samoan Passage in 2012–13 showed a small (0.5 ± 0.6 Sv) decrease in the northward transport of deep water from that in 1992–1994 (Voet et al. 2016). Voet et al. (2016) noted that this reduction is uncertain, but consistent with the decline of the northward geostrophic current at 32°S and the slowdown of the Pacific meridional overturning circulation (PMOC) in recent decades suggested by several indirect estimates (Kouketsu et al. 2011; Sloyan et al. 2013).

Heuze et al. (2015) compared the northward transport of deep water from the Southern Ocean to the Pacific Ocean for 24 climate models in the Coupled Model Intercomparison Project Phase 5 (CMIP5). They found a large discrepancy among the models, ranging from 1 to 17 Sv at 30°S in a long-term average (1986–2005). This discrepancy indicates our lack of quantification of the processes controlling the deep Pacific Ocean circulation. Since the deep Pacific Ocean circulation is associated with upwelling of seawater, we need to quantify the impact of processes by

✉ Takao Kawasaki
kawasaki@aori.u-tokyo.ac.jp

[1] Atmosphere and Ocean Research Institute, The University of Tokyo, Kashiwa, Japan

[2] Department of Marine Science and Technology, Fukui Prefectural University, Obama, Japan

which deep water gains buoyancy in controlling the deep Pacific Ocean circulation.

Turbulent mixing, induced by tides rather than winds, has been considered to be one of the most important among such processes (Munk and Wunsch 1998; Furuichi et al. 2008). Internal tides dissipate their energy to induce turbulent mixing either near the site of their generation (near-field mixing) or after propagating far (far-field mixing). The near-field mixing takes place near rough topography, as observed by microstructure measurements (e.g., Polzin et al. 1997; St. Laurent et al. 2001), and is the focus of many previous modeling studies (Hasumi and Suginohara 1999; Simmons et al. 2004; Kawasaki and Hasumi 2010). This mechanism has already been taken into account in most ocean models participating in the CMIP Phase 6 (e.g., Melet et al. 2013; Griffies et al. 2016).

Although the importance of the far-field mixing has long been pointed out, the number of studies and CMIP6 models explicitly incorporating its effect into ocean modeling is still small (e.g., Oka and Niwa 2013; Melet et al. 2016; Voldoire et al. 2019). Oka and Niwa (2013; hereafter ON13) incorporated the far-field mixing into a realistically configured OGCM and found that the far-field mixing has a significant impact on the deep Pacific Ocean circulation. They calculated vertical diffusivity (κ_V) by

$$\kappa_V = \kappa_b + \Gamma \frac{E_{NEAR}(x, y) F_{NEAR}(z)}{\rho_0 N^2} + \Gamma \frac{E_{FAR}(x, y) F_{FAR}(z)}{\rho_0 N^2}, \tag{1}$$

where κ_b ($= 10^{-5} \mathrm{m}^2\,\mathrm{s}^{-1}$) is background vertical diffusivity. E_{NEAR} and E_{FAR} are the column-integrated rates of tidal energy dissipation (conversion rate from internal-tide energy to small-scale turbulent kinetic energy) for the near- and far-fields, respectively, calculated by a high resolution numerical model of tides (Niwa and Hibiya 2011). Other variables in Eq. (1) will be described later (in Sect. 2.2). The vertical structure–function of far-field mixing was chosen simply as a constant such that its vertical integration becomes unity ($F_{FAR}(z) = 1/z_b$; where z_b is the depth of bottom) in ON13. However, many previous observational and theoretical studies have suggested that the far-field dissipation rate is proportional to the squared Brunt-Vaisala frequency (e.g., Gargett and Holloway 1984; Henyey et al. 1986; Gregg and Sanford 1988; Kunze 2017). This relationship between energy dissipation rate and stratification is consistent with a recent microscale observation (Goto et al., submitted).

On the other hand, several previous modeling studies pointed out the importance of geothermal heating as a source of buoyancy for the deep water in the Pacific Ocean (e.g., Hofmann and Morales Maqueda 2009; Emile-Geay and Madec 2009; Urakawa and Hasumi 2009). However, most of the CMIP5 models did not incorporate its effect.

In the present study, we investigate the control factors of the deep Pacific Ocean circulation by conducting a series of numerical experiments. Compared with previous studies, we update the method for estimating both the near- and far-field mixing. Besides, here we use the modeled stratification (not observed climatology) in determining the vertical diffusivity and apply the geothermal heating, neither of which is the case in ON13.

The description of the model and experiment design will be given in Sect. 2. In Sect. 3, the result of the model will be shown, where we will especially focus on the PMOC and the distribution of radiocarbon in the Pacific Ocean. The differences from the results obtained by ON13 are also discussed in this section. Finally, a summary and discussions on these results are presented in Sect. 4.

2 Model description

2.1 Ocean general circulation model (OGCM)

The ice-ocean coupled model utilized in the present study is COCO. This model is used as the ocean component of the Model for Interdisciplinary Research on Climate, version 6 (MIROC6; Tatebe et al. 2019), which is developed for CMIP phase 6 (CMIP6). The model domain is global and the tripolar coordinate is employed as a horizontal grid system. The horizontal grid size is 1 degree. The model is configured with 62 vertical levels, and the grid spacing varies from 2 (top) to 660 m (bottom: 7200 m). The second-order moments conserving scheme is utilized to calculate the tracer advection (Prather 1986). A turbulence closure scheme of Noh and Kim (1999) is applied for diagnosing vertical viscosity and diffusivity near the sea surface. The model incorporates the isopycnal diffusion (Cox 1987), and isopycnal layer thickness diffusion (Gent et al. 1995), where their coefficients are 1.0×10^3 and 3.0×10^2 $\mathrm{m}^2\,\mathrm{s}^{-1}$, respectively. The model is driven by the climatological monthly-mean sea surface forcing of Röske (2001), which is derived from the 1979–1993 ECMWF Re-analysis data-set (Gibson et al. 1997). To avoid a drift in salinity and unrealistic weakening of the Atlantic meridional overturning circulation, sea surface salinity is weakly (the time constant is 30 days for 2-m thickness) restored to a monthly mean climatology (Polar Science Center Hydrographic Climatology PHC version 3.0; Steele et al. 2001).

2.2 Parameterization of tide-induced vertical mixing

The vertical diffusivity is calculated by the Osborn (1980)'s formula:

$$\kappa_V = \Gamma \frac{E_{NEAR}(x,y)F_{NEAR}(z) + E_{FAR}(x,y)F_{FAR}(z)}{\rho_0 N^2}, \quad (2)$$

where Γ is the mixing efficiency assumed to be 0.2 (St. Laurent and Schmitt 1999), ρ_0 is the constant reference density of seawater ($= 10^3 \mathrm{kgm}^{-3}$), and N is the Brunt-Väisälä frequency. This formula is similar to that utilized in ON13 (Eq. 1) except for the absence of the background mixing. Figure 1 shows the global maps of column-integrated energy dissipation rates for the near- and far-fields (E_{NEAR} and E_{FAR}) incorporated in our model. They are constructed by horizontally averaging the result of a 1/20° resolution tide model (Niwa and Hibiya 2014), which is similar to the data employed in ON13. Niwa and Hibiya (2014) demonstrated the dependency of the energy conversion rates from barotropic to baroclinic tides on the horizontal grid size of the tide model and suggested an extrapolation to the limit of zero grid spacing. Based on this extrapolation, the tidal dissipation rates are uniformly increased by 20% (50% in ON13). Consequently, the globally integrated dissipation rate is 1.08 TW, which is consistent with the estimate based on satellite-altimeter (Egbert and Ray 2000) and almost the same as that in ON13.

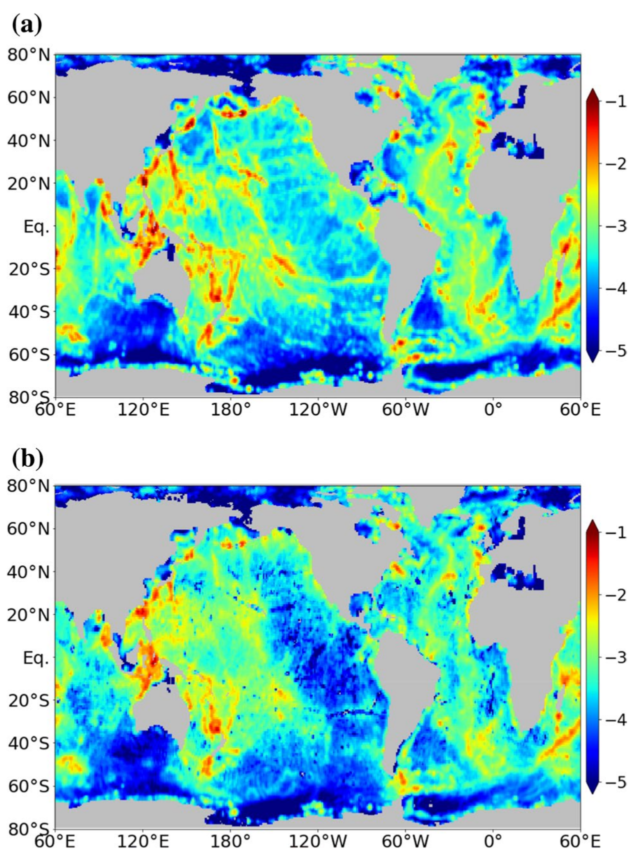

Fig. 1 The 1-degree global maps of column-integrated energy dissipation rates for **a** near- and **b** far-fields ($\log_{10}[E_{NEAR}(\mathrm{Wm}^{-2})]$ and $\log_{10}[E_{FAR}(\mathrm{Wm}^{-2})]$, respectively) incorporated into the ocean model

From the output of the tide model, the energy conversion rate (E_C) from barotropic tides to baroclinic tides and the energy dissipation rate (E_D) of baroclinic tides at each horizontal point are determined. Here, E_D is the sum of E_C and the horizontal convergence of internal tide energy flux ($\boldsymbol{F}$), (i.e., $E_D = E_C - \nabla \bullet \boldsymbol{F}$). E_D includes the contributions from the locally generated internal tides (E_{NEAR}) and the far propagated internal tides (E_{FAR}). If the baroclinic tidal energy converges ($\nabla \bullet \boldsymbol{F} < 0$), all of the generated baroclinic tidal energy is assumed to be locally dissipated ($E_{NEAR} = E_C$), and the convergence of baroclinic tidal energy is regarded as the far-field mixing ($E_{FAR} = -\nabla \bullet \boldsymbol{F}$). Otherwise, the whole of E_D is considered to be accounted for by the locally generated internal tides ($E_{NEAR} = E_D$), and no contribution from distantly propagated internal tides is assumed ($E_{FAR} = 0$). The globally integrated E_{NEAR} and E_{FAR} are 650 and 433 GW, respectively, after the 20% increase described above, and the global (power-weighted) average of local dissipation efficiency ($q = E_{NEAR}/E_C$) becomes ~ 0.6 by our method. This is much larger than the value assumed in previous studies ($q = 0.3$) (e.g., Egbert and Ray 2001; St. Laurent et al. 2002). However, a recent semi-analytical model of internal tide generation combined with satellite and turbulence observations suggested that q spatially varies and the power-weighted global average becomes 0.49 (Vic et al. 2019). This suggests that our way of partitioning the tidal energy dissipation rate into E_{NEAR} and E_{FAR} is not completely artificial.

Note that the tide model dissipates tidal energy by the ad hoc damping term of baroclinic fluctuations by the constant time scale of 30 days (Niwa and Hibiya 2014). This assumption could lead to inaccuracies in energy propagation processes and horizontal distribution of the far-field mixing (Fig. 1b). For instance, although 30 days is comparable to the propagation time scale for the 1st mode of crossing the Pacific Ocean, the far-field mixing energy in the eastern Pacific Ocean can be underestimated due to the lack of contribution from the 2nd and higher mode tidal waves.

The vertical profile of the dissipation rate in the near-field (F_{NEAR}) is the same as the previous studies (St. Laurent et al. 2002; ON13):

$$F_{NEAR}(z) = \frac{\exp\left[-\left(z_b - z\right)/\zeta\right]}{\zeta\left(1 - \exp\left[-z_b/\zeta\right]\right)}, \quad (3)$$

where z_b is the depth of the bottom. The dissipation rate is assumed to decay exponentially away from the bottom with a scale height of ζ. The seemingly complex formula in the denominator on the right-hand side is the normalization factor. St. Laurent et al. (2002) set ζ to 500 m based on turbulent observation in limited areas (St. Laurent et al.

2001). However, other observational studies suggested that the vertical structure of the dissipation rate varies spatially (e.g., Decloedt and Luther 2012; Waterhouse et al. 2014). Eikonal calculations suggested that the vertical decay scale tends to increase over rough bathymetry, where the amplitude of the tidal current is large (Hibiya et al. 2017). This result is qualitatively consistent with the map of vertical decay scale ζ in the recently suggested parameterization of tidal mixing (de Lavergne et al. 2020), in which the vertical decay scale exceeds 500 m, where E_{NEAR} is large (e.g., the Izu-Ogasawara Ridge, the Hawaiian Ridge, and the Ryukyu Island chain; Fig. 1a). Based on these previous studies, we investigate the sensitivity of the deep Pacific Ocean circulation to ζ by choosing either 500 m or 1000 m (uniform values) in this study.

Many previous studies showed that the dissipation rates far from the generation sites are proportional to the squared Brunt-Väisälä frequency (e.g., Gargett and Holloway 1984; Kunze 2017). This fact has consistency with a recent turbulence observation (Goto et al. 2020 submitted). Following these results, we assume the same vertical profile of far-field energy dissipation rate as in previous studies (Melet et al. 2016; de Lavergne et al. 2020):

$$F_{\mathrm{FAR}}(z) = \frac{N^2}{\int_{-z_b}^{0} N^2 \mathrm{d}z}. \tag{4}$$

Here, the vertical profile is estimated using the simulated potential temperature and salinity at every time step.

It should be noted that the E_{NEAR} is the local full-water-column dissipation rate, because E_{NEAR} and E_{FAR} are both calculated based on the horizontal divergence/convergence of energy propagation. Here, the entirety of E_{NEAR} is distributed as an exponential decay from the seafloor upwards (Eq. 3). In reality, a sizeable fraction of E_{NEAR} may contribute to mixing in the stratified upper ocean, with a strong dependence on N^2 as in Eq. (4) (Kunze et al. 2006; Polzin 2009; Lefauve et al. 2015). Thus, our assumption that all of E_{NEAR} enhances the bottom-intensified mixing could lead to an overestimate of effects of mixing near the bottom and an underestimate of the effects of mixing in the stratified upper ocean.

2.3 Experimental design

We conducted several experiments to examine the sensitivity of the PMOC to several controlling factors (Table 1). In our control experiment (CTRL), the decay scale of near-field mixing from the bottom is set to 500 m, which is the same as many previous studies (e.g., St. Laurent et al. 2002, ON13). A global map of the geothermal heating at the sea-floor is applied (Davies 2013). The experiments CONST, NoFAR, 1000M, NoGTHM are conducted to clarify the sensitivity to the vertical profile of the far-field mixing, existence of the far-field mixing, the decay scale of near-field mixing, and presence/absence of geothermal heating, respectively. For instance, in the experiment NoFAR, the experimental procedure is the same as for the experiment CTRL except that the internal-tidal energy that propagates away from the generation sites disappears: E_{FAR} is set to zero everywhere, and $E_{\mathrm{NEAR}} = E_{\mathrm{C}} - \nabla \bullet \boldsymbol{F}$, where $\nabla \bullet \boldsymbol{F} > 0$. Offline Δ^{14}C experiments under the monthly mean circulation and mixing fields with nudging to natural Δ^{14}C (Key et al. 2004) at the sea surface are also conducted to evaluate the deep Pacific Ocean circulation using the same method as in ON13. All experiments are conducted with more than 6000 years of spin-up to calculate steady states of the PMOC and Δ^{14}C, and the last 100 years of the integral period are examined in this study.

3 Results

3.1 Pacific meridional overturning circulation (PMOC)

The PMOC is expressed as the zonally integrated stream function within the Pacific sector (Fig. 2). The dense water originated from the Southern Ocean is transported northward in the lower deep layer (> ~ 3500 m depth) in all experiments. Some of the deep water returns to the Southern Ocean in the upper deep layer (~ 2000–3500 m depth) and the remaining deep water upwells within the Pacific Ocean and reaches the intermediate or shallow layer (< 2000 m depth).

Table 1 Experimental list in the present study. The bolded text indicates the difference from the control experiment (CTRL) in each experiment

Experiment Name	Vertical profile of far-field mixing	Far-field mixing	Decay scale of near-field mixing	Geo-thermal heating
CTRL	Prop. to N^2	ON	500 m	ON
CONST	**Const**	ON	500 m	ON
NoFAR	N/A	**OFF**	500 m	ON
1000M	Prop. to N^2	ON	**1000 m**	ON
NoGTHM	Prop. to N^2	ON	500 m	**OFF**

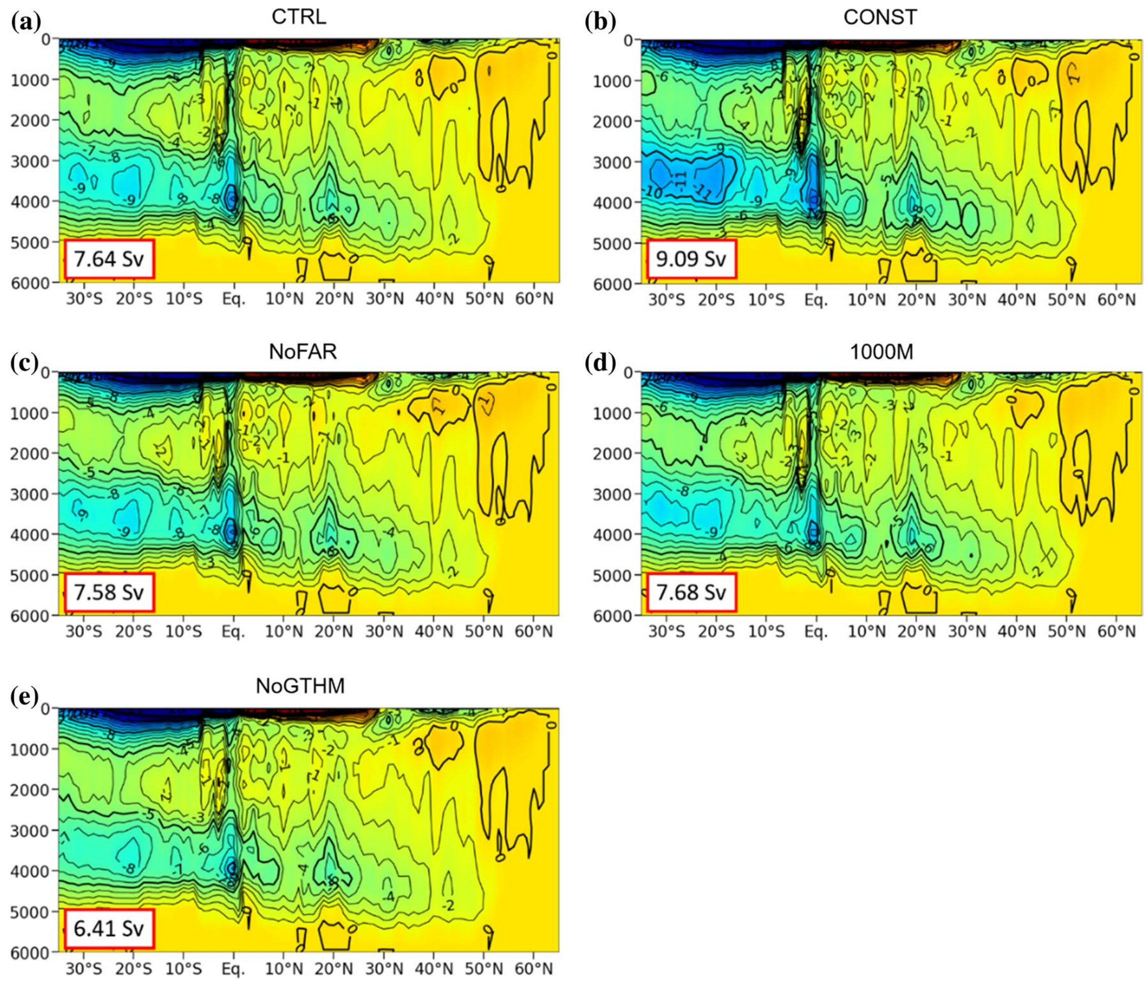

Fig. 2 The zonally integrated stream function in the Pacific Ocean in **a** CTRL, **b** CONST, **c** NoFAR, **d** 1000M, and **e** NoGTHM. Positive for clockwise circulation. The thick and thin contour intervals are 5 and 1 Sv, respectively. The number in the red box shown at the left-bottom corner is the northward volume transport at the Samoan Passage and its adjacent pathways (~10°S) in the lower deep layer (deeper than 3500 m). It should be mentioned that the discontinuities in the stream function and upwelling in the shallow layer (above ~1000 m depth) around the equator indicate the Indonesian Throughflow and its associated circulation. This structure does not directly influence the deep ocean circulation focused on in this study

The northward volume transport at 10°S (hereinafter referred to as T10S) in the lower deep layer (> 3500 m depth), which means the total northward transport through the Samoan Passage and its adjacent pathways (e.g., the Penrhyn Basin), is 7.64 Sv in the control experiment (CTRL) (Fig. 2a). This value is smaller than the estimate from mooring measurements (~9–10 Sv; Rudnick 1996; Voet et al. 2016). The discrepancy is discussed in the following sections.

The experiment CONST adopts the same method to estimate the vertical distribution of the far-field mixing as ON13, where the energy dissipation rate for the far-field mixing is vertically uniform. The T10S is 9.09 Sv in the experiment CONST (Fig. 2b). ON13 obtained 8 Sv as the deep extremum of the PMOC stream function at the equator, which is almost the same as T10S (Fig. 2e in ON13). Considering the lack of geothermal heating (which accounts for about 1 Sv in T10S as described later) in ON13, this experiment seems to reproduce that by ON13 well.

To relate T10S to the tide-induced vertical mixing, the total vertical volume transport and the total dissipated energy in the north of 10˚S are shown in Fig. 3. The northward transport in the lower deep layer and its upwelling to the upper deep layer significantly increase (by 1.45 Sv), and the intensified upwelling extends to ~1000 m depth in the experiment CONST (Figs. 2b, 3a, c). The enhanced (weakened) upwelling in the deep (shallow) layer corresponds to the increase (decrease) of the energy dissipation rate for the far-field mixing (Fig. 3).

Absence of far-field mixing (the experiment NoFAR) does not significantly decrease the northward transport of deep water, because the dissipation rate for far-field mixing

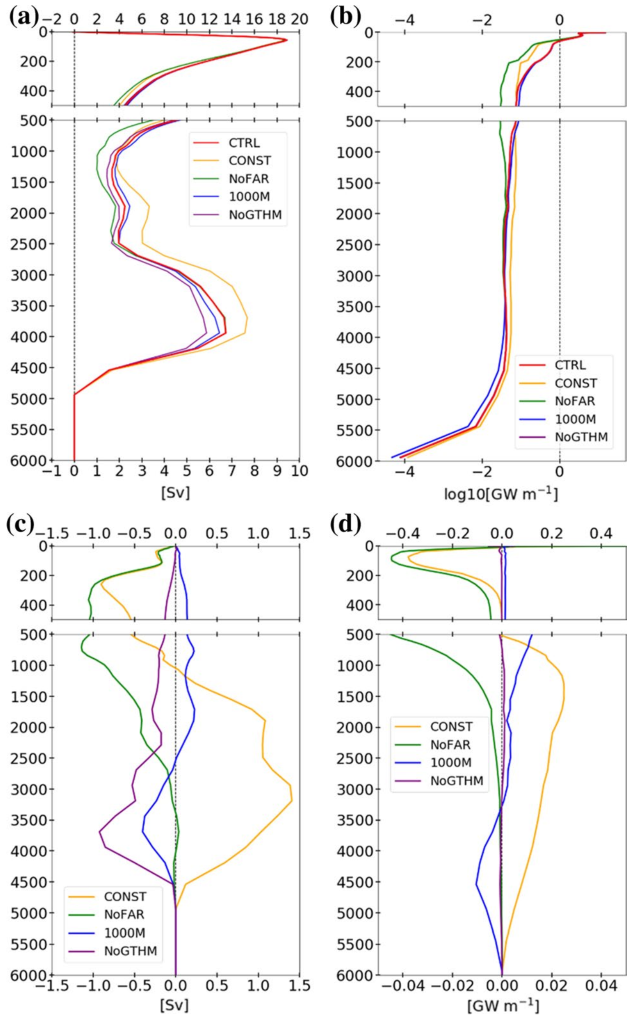

Fig. 3 Horizontally integrated **a** volume transport (unit is Sv) and **b** tidal energy dissipation rate (unit is GW $m^{-1} = 10^9$ W m^{-1}) in the north of 10°S in the Pacific Ocean. **c**, **d** are the same as **a** and **b** but the difference from the control experiment (CTRL) in each experiment, respectively. Note that the horizontal scale in **a** and **d** is different between the upper and lower panels. Note that the dissipation rate for NoGTHM is almost invisible in **b,** because the line overlaps that for CTRL

in the lower deep layer is quite small in the experiment CTRL (Figs. 2c and 3). On the other hand, the upwelling from the upper deep layer to the shallow layers becomes weak without the far-field mixing in the Pacific Ocean (Fig. 3a, c). Since the magnitude of far-field mixing in the experiment CTRL is large, where the stratification is strong, its influence is limited to the upper layer (Fig. 3). The weak sensitivity of the northward transport of deep water to far-field mixing, whose vertical profile depends on the stratification, is consistent with previous studies (sensitivity in a coupled model with an isopycnal ocean model, Melet et al. 2016; calculation based on the climatological stratification, de Lavergne et al. 2016).

Note that ON13 estimated that the vertically constant far-field mixing increases the northward transport of deep water in the Pacific Ocean by 4 Sv (case TideNF—case TideN in their paper). On the other hand, an increase of only 1.5 Sv is estimated in our model (CONST—NoFAR). The possible underestimate of far-field mixing by our parameterization could lead to the small influence of far-field mixing on the deep water transport.

When the decay scale height of near-field mixing is raised to 1000 m (the experiment 1000M), the total northward transport of deep water in the lower deep layer (> 3500 m) and its upwelling to the upper deep layer slightly decrease (by 0.35 Sv; Fig. 3a, d). It corresponds to the decrease of the dissipation rate for near-field mixing in the lower deep layer (Fig. 3b, d). It is noted that despite this slight difference in the upwelling of deep water, the T10S is almost the same as that in the experiment CTRL. This slight difference is related to the weak abyssal currents in the east of the Penrhyn Basin. The small sensitivity of the northward transport of deep water on the vertical decay scale is consistent with the estimate of water mass transformation based on the hydrographic climatology (de Lavergne et al. 2016). Conversely, upwelling increases in the upper layers corresponding to the enhanced mixing (Fig. 3).

Removal of the geothermal heat leads to a reduction of T10S by 1.23 Sv (Fig. 2a, e). Thus, upwelling is strongly intensified by geothermal heating in the lower and upper deep layers in the Pacific Ocean. The quantitative impact of geothermal heating is consistent with previous modeling studies (Hofmann and Morales Maqueda 2009; Emile-Geay and Madec 2009).

Note that vertical profiles of the employed tidal dissipation rate in CTRL exhibit an increase from the deep layer to the thermocline over the Izu-Ogasawara Ridge, Hawaiian Ridge, and Fieberling Guyot, whereas all profiles exhibit a decrease in CONST and NoFAR (figure not shown). This increase of tidal dissipation rate in CTRL is consistent with available microstructure measurements in the North Pacific Ocean compiled by de Lavergne et al. (2020). Note that some model profiles show excessive bottom intensification compared to observation. This discrepancy may be due to the aforementioned potential overestimation of the near-bottom dissipation.

3.2 Validation using $\Delta^{14}C$

To evaluate the validity of the constructed map of tidal mixing and the obtained strength of the deep Pacific Ocean circulation, we employed $\Delta^{14}C$ which is an indicator of how long it has taken, since seawater is isolated from contact with the atmosphere. We use a gridded dataset of observed climatology of $\Delta^{14}C$ (GLODAPv2 dataset; de Lavergne et al. 2017) for a comparison purpose. This dataset is not bomb-corrected but constructed by isopycnal averaging and includes many more measurements than that of the previous GLODAP dataset (Key et al. 2004), leading to more reliable maps (de Lavergne et al. 2017). It should be mentioned that the ventilation timescale is sufficiently long that the influence of bomb Δ^{14}C should be very small in the deep (> 1500 m depth) Pacific Ocean north of 30°S. The Δ^{14}C along the central Pacific meridional section (170°W), which includes the Samoan Passage, is shown in Fig. 4. As the selected meridional section is mostly along one of the survey lines, the estimated error of gridded data is relatively small (Key et al. 2004). In all experiments, relatively young water from the Southern Ocean gets older as it moves northward in the lower deep layer (Fig. 4). The seawater in the upper deep layer (2000–3500 m depth) is the oldest in the World Ocean. The extremal value of Δ^{14}C in the upper deep layer is controlled by the northward and upward transports in the lower deep layer and vertical mixing with the younger water in the upper layer.

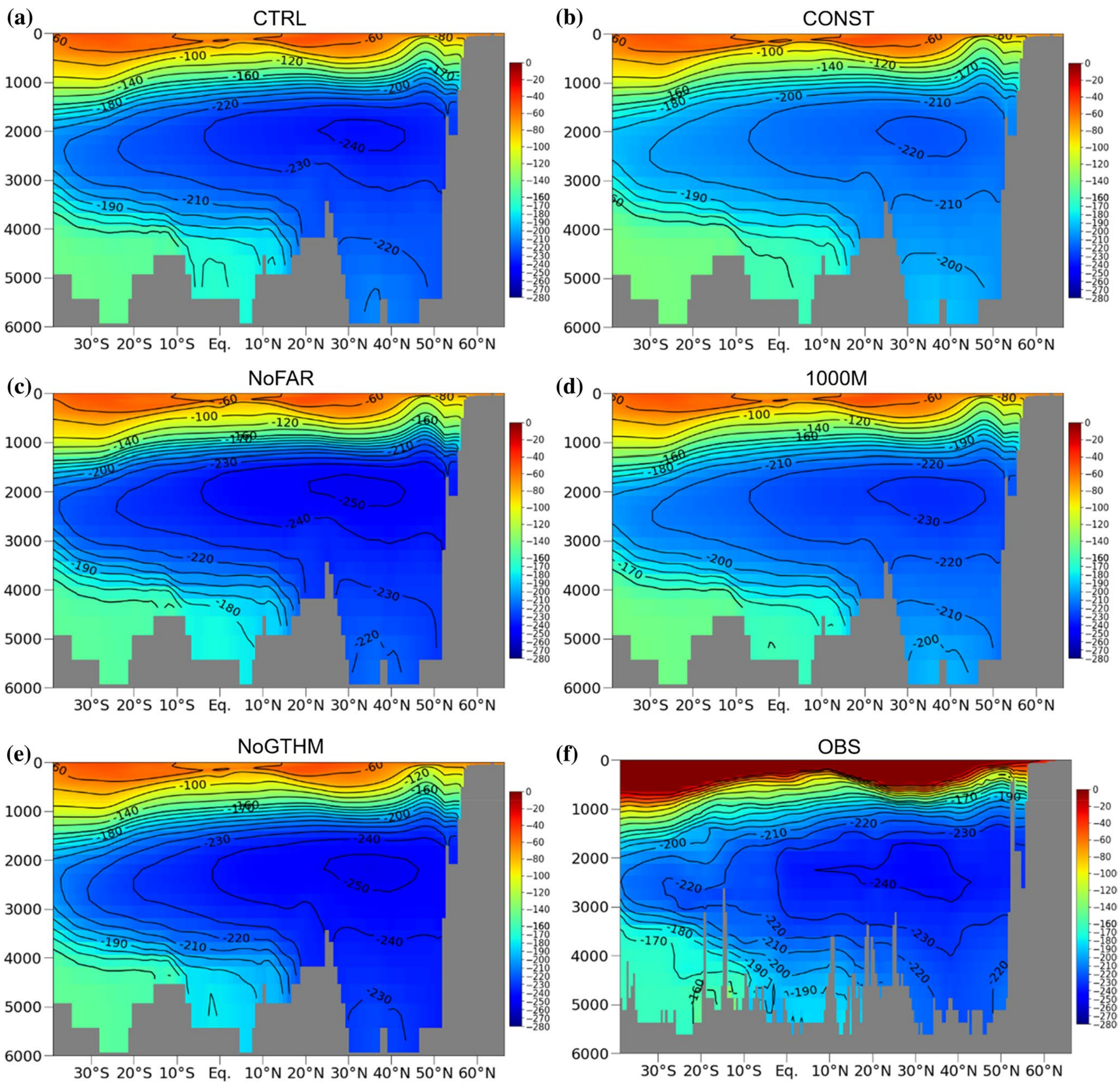

Fig. 4 The meridional section of Δ^{14}C along 170°W in **a** CTRL, **b** CONST, **c** NoFAR, **d** 1000M, and **e** NoGTHM. **f** The same section of the climatological data constructed through the Global Ocean Data Analysis Project Version 2 (GLODAP v2; de Lavergne et al. 2017). The unit is ‰. Contour intervals are 20 and 10 ‰ for more and less than − 160 ‰, respectively

In the experiment NoGTHM, since the T10S is smaller, the water in the upper deep layer is older than that in CTRL (Figs. 2a, e, 4a, e). Despite no large difference in the T10S between NoFAR and CTRL (Fig. 2a, c), the difference in $\Delta^{14}C$ is comparable to the other cases (e.g., NoGTHM; Fig. 4). Similarly, the difference in $\Delta^{14}C$ between 1000M and CTRL is not associated with the difference in T10S (Figs. 2a, d, 4). Because the northward transport of deep water is hardly influenced by the existence of far-field mixing and the change in the decay scale height of near-field mixing, the water age in the upper deep layer is controlled by the mixing with the shallower water (Fig. 2c, d). In NoFAR (1000M), since the tidal energy dissipation rate is smaller (larger) in the shallow, intermediate, and upper deep layers, the water in the upper deep layer is older (younger) than that in the experiment CTRL (Figs. 3d, 4c, d). In the experiment CONST, since both the T10S and vertical mixing within the shallow and upper deep layers are larger than those in CTRL (Figs. 2a, b, 3d), the water in the upper deep layer is younger than that in CTRL (Fig. 4a, b).

The horizontal distribution of $\Delta^{14}C$ at the 2500 m depth, where the oldest water exists in the North Pacific Ocean, shows that the location of the oldest water is consistent with the observation in all experiments (Fig. 5). The minimum $\Delta^{14}C$ (age of the oldest water) is better reproduced in the experiments CTRL and NoFAR (Fig. 5a, c, f). The $\Delta^{14}C$ in the western Pacific Ocean, where the youngest water exists in the North Pacific Ocean, is simulated better in CTRL and 1000M (Fig. 5a, d, f). On the other hand, the seawater becomes too old in the upper deep layer without the geothermal heating or far-field mixing (Fig. 5c, e, f). Compared with the youngest and oldest waters exhibited in the observational climatology, we can judge that $\Delta^{14}C$ in both the western and northeastern Pacific Ocean is best reproduced in the experiment CTRL (Fig. 5a, f).

4 Summary and discussion

In this study, we introduce improved methods for parameterizing tidal mixing to investigate the control mechanisms of deep Pacific Ocean circulation. The column-integrated dissipation rates in near- and far-fields are calculated from the rates of energy conversion from barotropic to baroclinic tides and from baroclinic tide to turbulence, respectively, estimated by a high resolution tide model. The dependency of the far-field mixing on stratification is also considered based on long-standing theoretical and observational knowledge. The far-field mixing does not have a significant effect on the deep Pacific Ocean circulation compared to a previous study (ON13) that did not consider its dependency on stratification. The deep Pacific Ocean circulation is not sensitive to the decay scale height of the near-field mixing. But it is found that the reproducibility of the radiocarbon, especially its extremal value in the upper deep layer, is affected by these factors through the mixing with the shallower layers. It should be noted that there is considerable uncertainty in the distribution of the near- and far-field dissipation rates, because of the limitations of the high resolution model simulation and the simplifying assumptions in the chosen vertical structures of dissipation.

The northward volume transport in the deep Pacific Ocean is underestimated in our model compared with the mooring observations except for in the experiment CONST (Fig. 2). However, vertically uniform rates of dissipation for the far-field mixing assumed in the experiment CONST are inconsistent with many previous studies which suggest its dependency on stratification (e.g., Gargett and Holloway 1984; Gregg and Sanford 1988; Kunze 2017; Goto et al. 2020 submitted). On the other hand, the minimum of $\Delta^{14}C$ in the upper deep Pacific Ocean is reproduced well in the experiment CTRL (and also the experiments 1000M and NoFAR; Fig. 5), which suggests that the northward volume transport in the deep Pacific Ocean may also be reproduced well in the experiment CTRL. But the values of simulated $\Delta^{14}C$ for the water entering the deep Pacific Ocean from the Southern Ocean are slightly high compared with the observation (Fig. 4). This may indicate that the simulated residence time of deep water in the Pacific Ocean is too long and thus the vertical mixing with upper water is too weak or the simulated northward volume transport in the deep Pacific Ocean is too small. Note that a diagnostic model on global thermohaline circulation suggested that mesoscale eddy diffusion influences the distribution of $\Delta^{14}C$ in the deep Pacific Ocean (Holzer and Primeau 2006). Thus, the uncertainty of eddy parameterization (isopycnal diffusivity) could also cause the bias of $\Delta^{14}C$ in our model. It is not conclusive at this stage whether the deep Pacific Ocean volume transport is reasonably simulated or underestimated in the experiment CTRL (or in the other experiments).

There still is a possibility that the observed volume transport based on mooring is an overestimate as a long-term mean. The duration of each mooring is 1.5 years, and its time series exhibits a variability of ± 2 Sv on seasonal to interannual timescales. Although the difference between the estimates based on the two mooring observations conducted in 1992–1994 and 2012–2013 is small (0.5 Sv), this does not exclude a possibility of the existence of large variability in the volume transport on interannual and longer timescales. An analysis of climate models shows 2–3 Sv for the interannual standard deviation of the PMOC transport (Tandon et al. 2020), which supports the existence of large variability in the volume transport in the deep Pacific Ocean.

If we accept the estimates based on mooring as the long-term mean transport, there should be some sources of buoyancy which are left untreated in our model. One of the

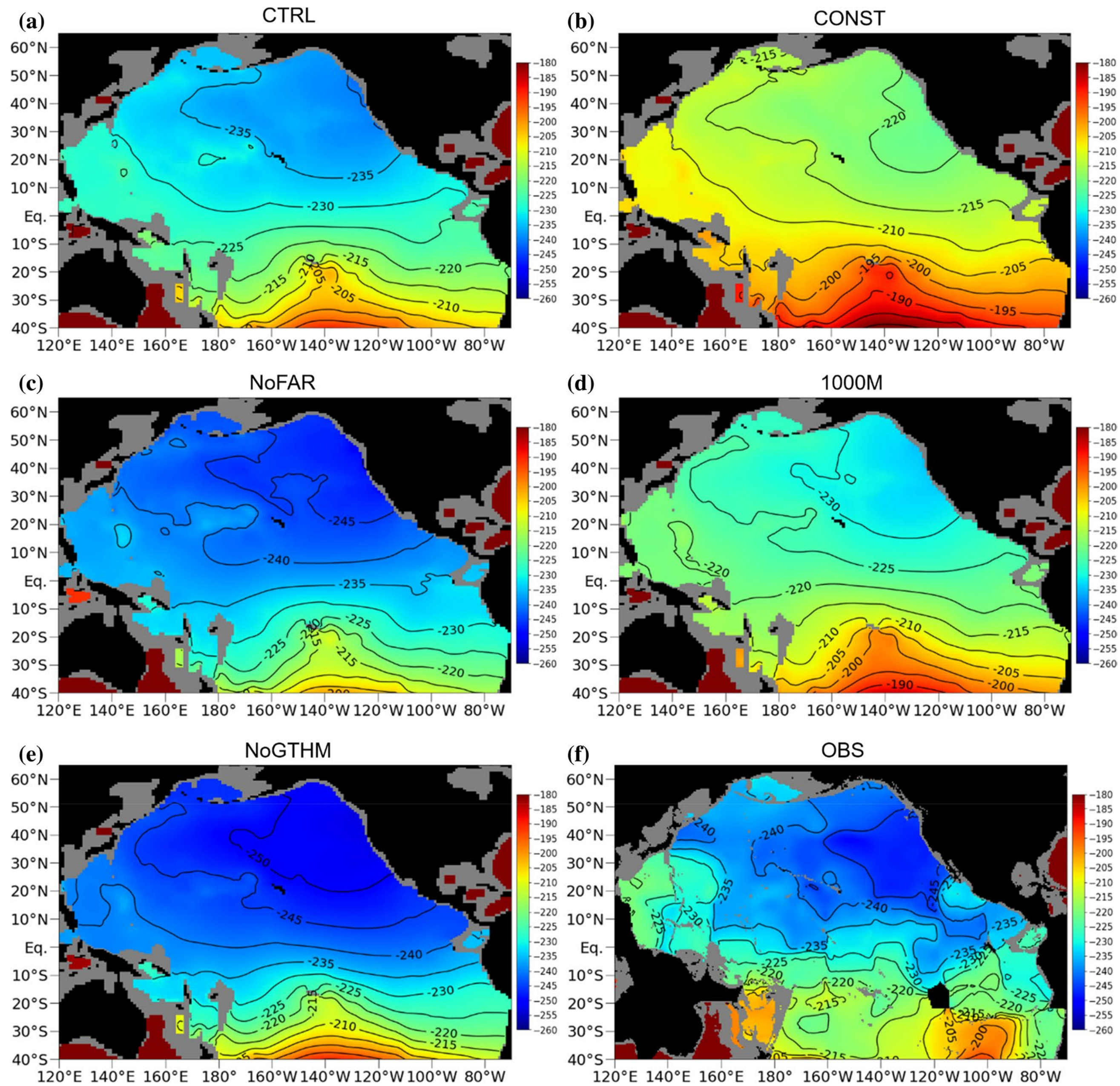

Fig. 5 Same as Fig. 4, but the horizontal distribution of Δ^{14}C at 2500 m depth. The contour interval is 5 ‰

candidates is the dissipation of far-propagating internal tides at continental slopes (Kelly et al. 2013; Eden and Olbers 2014). We conducted an additional experiment to investigate its impact. Since the high-resolution tide model, on which our estimates of E_{NEAR} and E_{FAR} is based, contains such far-propagating internal tides, some of its effects are already incorporated in the CTRL experiment through E_{FAR} at the model grid points adjacent to lateral boundaries (continental slopes). However, the true vertical profile of continental-slope dissipation does not have a dependency with the stratification as in Eq. (4) but is rather bottom-intensified (e.g., Moum et al. 2002; Nash et al. 2004). Thus, in this additional experiment, to increase the impact of this mixing further by enhancement of deep-ocean mixing rather than upper-ocean mixing, E_{FAR} at continental slopes is uniformly distributed in the vertical ($F_{\mathrm{FAR}}(z) = 1/z_{\mathrm{b}}$, where z_{b} is the depth of bottom). Here, the continental slopes are defined as the grid points, where $z_{\mathrm{b}} > 250$ m and within 200 km from the continental shelves, which are defined as the grid points, where $z_{\mathrm{b}} < 250$ m. The result shows that the deep Pacific Ocean circulation is little influenced by vertically homogenized mixing at continental slopes (figure not shown). It should be noted that the far-field dissipation rates on the continental slopes may be underestimated when the ad hoc damping of baroclinic fluctuations is too large in the tide model. The underestimation is especially pronounced if the arrival of internal waves of the second and subsequent low modes is significant on the continental slopes. The dissipation rate is also underestimated, where small (sub-grid) scale topography causes efficient dissipation on the continental slopes.

We did not take account of the mixing due to wind-induced internal waves as the distribution of its energy calculated by a full three-dimensional primitive equation model suggests its insignificance in the deep ocean (Furuichi et al. 2008). However, a recent analysis of Argo profiling floats found that winds enhance mixing at least to the depth of 2000 m in regions of strong eddy activity such as around the Kuroshio and its Extension (Whalen et al. 2018). To properly incorporate its effect into models, we need a resolution significantly higher than that employed in this study.

Model resolution might affect the deep Pacific Ocean circulation from another point of view. North Pacific Intermediate Water (NPIW) and the associated circulation in the Pacific Ocean intermediate layer are not sufficiently represented in models unless a significantly high resolution is employed (Ishikawa and Ishizaki 2009). This circulation pushes down buoyancy and high $\Delta^{14}C$ from the surface layer to the intermediate layer. Therefore, its proper representation in models may lead to higher buoyancy gain of the deep water, and thus stronger deep circulation, and higher deep-water $\Delta^{14}C$ in the Pacific Ocean.

Acknowledgements This work is supported by the JSPS MEXT KAKENHI Grant Number JPH05825. This research was conducted using the Fujitsu PRIMERGY CX600M1/CX1640M1 (Oakforest-PACS) in the Information Technology Center, The University of Tokyo. All figures are drawn using the libraries of the Python (e.g., NumPy, Matplotlib).

References

Cox MD (1987) Isopycnal diffusion in a z-coordinate ocean model. Ocean Model 74:1–5

Davies JH (2013) Global map of solid Earth surface heat flow. Geochem Geophys Geosys 14(10):4608–4622. https://doi.org/10.1002/ggge.20271

de Lavergne C, Madec G, Sommer JL, Nurser AJG, Naveira-Garabato AC (2016) On the consumption of antarctic bottom water in the abyssal ocean. J Phys Oceanogr 46:635–661. https://doi.org/10.1175/JPO-D-14-0201.1

de Lavergne C, Madec G, Roquet F, Holmes RM, McDougall TJ (2017) Abyssal ocean overturning shaped by seafloor distribution. Nature 551:181–186. https://doi.org/10.1038/nature24472

de Lavergne C, Vic C, Madec G, Roquet F, Waterhouse AF, Whalen CB, Cuypers Y, Bouruet-Aubertot P, Ferron B, Hibiya T (2020) A parameterization of local and remote tidal mixing. J Adv Model Earth Sys. https://doi.org/10.1029/2020MS002065

Decloedt T, Luther DS (2012) Spatially heterogeneous diapycnal mixing in the abyssal ocean: a comparison of two parameterizations to observations. J Geophys Res 117:C11025. https://doi.org/10.1029/2012JC008304

Eden C, Olbers D (2014) An energy compartment model for propagation, nonlinear interaction, and dissipation of internal gravity waves. J Phys Oceanogr 44(8):2093–2106. https://doi.org/10.1175/JPO-D-13-0224.1

Egbert GD, Ray RD (2000) Significant dissipation of tidal energy in the deep ocean inferred from satellite altimeter data. Nature 93(1993):775–778

Egbert GD, Ray RD (2001) Estimates of M_2 tidal energy dissipation from TOPEX/Poseidon altimeter data. J Geophys Res 106(C10):22475–22502

Emile-Geay J, Madec G (2009) Geothermal heating, diapycnal mixing and the abyssal circulation. Ocean Sci 5:203–217

Furuichi N, Hibiya T, Niwa Y (2008) Model-predicted distribution of wind-induced internal wave energy in the world's oceans. J Geophys Res 113(6):1–13. https://doi.org/10.1029/2008JC004768

Gargett AE, Holloway G (1984) Dissipation and diffusion by internal wave breaking. J Mar Res 42:15–27. https://doi.org/10.1357/002224084788506158

Gent PR, Willebrand J, McDougall TJ, McWilliams JC (1995) Parameterizing eddy-induced tracer transports in ocean circulation models. J Phys Oceanogr 25:463–474

Gibson JK, Kallberg P, Uppala S, Hernandez A, Nomura A, Serrano E (1997) ERA Description. ERA Proj Rep 1, pp. 72, Eur Cent for Medium-Range Weather Forecasts, Reading, England

Goto Y, Yasuda I, Nagasawa M, Kouketsu S, Nakano T, Estimation of Basin-scale turbulence distribution in the North Pacific Ocean using CTD-attached thermistor measurements. Scientific Reports, in revision

Gregg MC, Sanford TB (1988) The dependence of turbulent dissipation on stratification in a diffusively stable thermocline. J Geophys Res 93(C10):12381–12392. https://doi.org/10.1029/jc093ic10p12381

Griffies SM, Danabasoglu G, Durack PJ, Adcroft AJ, Balaji V, Böning CW, Chassignet EP, Curchitser E, Deshayes J, Drange H, Fox-kemper B, Gleckler PJ, Gregory JM, Haak H, Hallberg RW, Heimbach P, Hewitt HT, Holland DM, Ilyina T, Jungclaus JH, Komuro Y, Krasting JP, Large WG, Marsland SJ, Masina S, McDougall TJ, Nurser G, Orr JC, Pirani A, Qiao F, Stouffer RJ, Taylor KE, Treguier AM, Tsujino H, Uotila P, Valdivieso M, Wang Q, Winton M, Yeager SG (2016) OMIP contribution to CMIP6: experimental and diagnostic protocol for the physical component of the Ocean Model Intercomparison Project. Geosci Model Dev. https://doi.org/10.5194/gmd-9-3231-2016

Hasumi H, Suginohara N (1999) Effects of locally enhanced vertical diffusivity over rough bathymetry on the world ocean circulation. J Geophys Res 104(C10):367–374

Henyey FS, Wright J, Flatte SM (1986) Energy and action flow through the internal wave field: an eikonal approach. J Geophys Res 91(C7):8487–8495

Heuze C, Heywood KJ, Stevens DP, Ridley JK (2015) Changes in global ocean bottom properties and volume transports in CMIP5 models under climate change scenarios. J Climate 28:2917–2944. https://doi.org/10.1175/JCLI-D-14-00381.1

Hibiya T, Ijichi T, Robertson R (2017) The impacts of ocean bottom roughness and tidal flow amplitude on abyssal mixing. J Geophys Res 122:5645–5651. https://doi.org/10.1002/2016JC012564

Hofmann M, Morales Maqueda M (2009) Geothermal heat flux and its influence on the oceanic abyssal circulation and radiocarbon distribution. Geophys Res Lett 36:L03603. https://doi.org/10.1029/2008GL036078

Holzer M, Primeau FW (2006) The diffusive ocean conveyor. Geophys Res Lett 33:L14618. https://doi.org/10.1029/2006GL026232

Ishikawa I, Ishizaki H (2009) Importance of eddy representation for modeling the intermediate salinity minimum in the North Pacific: comparison between eddy-resolving and eddy-permitting

models. J Oceanogr 65(3):407–426. https://doi.org/10.1007/s10872-009-0036-6
Kawasaki T, Hasumi H (2010) Role of localized mixing around the Kuril Straits in the Pacific thermohaline circulation. J Geophys Res. https://doi.org/10.1029/2010JC006130
Kelly SM, Jones NL, Nash JD, Waterhouse AF (2013) The geography of semidiurnal mode-1 internal-tide energy loss. Geophys Res Lett 40:4689–4693
Key RM, Kozyr A, Sabine CL, Lee K, Wanninkhof R, Bullister JL, Feely RA, Millero FJ, Mordy C, Peng TH (2004) A global ocean carbon climatology: results from Global Data Analysis Project (GLODAP). Global Biogeochem Cycles 18:1–23. https://doi.org/10.1029/2004GB002247
Kouketsu S, Doi T, Kawano T, Masuda S, Sugiura N, Sasaki Y, Toyoda T, Igarashi H, Kawai Y, Katsumata K, Uchida H, Fukasawa M, Awaji T (2011) Deep ocean heat content changes estimated from observation and reanalysis product and their influence on sea level change. J Geophys Res 116:1–16. https://doi.org/10.1029/2010JC006464
Kunze E (2017) Internal-wave-driven mixing: global geography and budgets. J Phys Oceanogr 47(6):1325–1345. https://doi.org/10.1175/JPO-D-16-0141.1
Kunze E, Firing E, Hummon JM, Chereskin TK, Thurnherr AM (2006) Global abyssal mixing inferred from lowered ADCP shear and CTD strain profiles. J Phys Oceanogr 36(8):1553–1576. https://doi.org/10.1175/JPO2926.1
Lefauve A, Muller C, Melet A (2015) A three-dimensional map of tidal dissipation over abyssal hills. J Geophys Res 120:4760–4777. https://doi.org/10.1002/2014JC010598
Lumpkin R, Speer K (2007) Global ocean meridional overturning. J Phys Oceanogr 37:2550–2562. https://doi.org/10.1175/JPO3130.1
Melet A, Hallberg R, Legg S, Polzin K (2013) Sensitivity of the ocean state to the vertical distribution of internal-tide-driven mixing. J Phys Oceanogr 43(3):602–615. https://doi.org/10.1175/JPO-D-12-055.1
Melet A, Legg S, Hallberg R (2016) Climatic impacts of parameterized local and remote tidal mixing. J Climate 29(10):3473–3500. https://doi.org/10.1175/JCLI-D-15-0153.1
Moum JN, Caldwell DR, Nash JD, Guderson GD (2002) Observations of boundary mixing over the continental slope. J Phys Oceanogr 32(7):2113–2130
Munk WH, Wunsch C (1998) Abyssal recipes II: Energetics of tidal and wind mixing. Deep Sea Res I 45:1977–2010
Nash JD, Kunze E, Toole JM, Schmitt RW (2004) Internal tide reflection and turbulent mixing on the continental slope. J Phys Oceanogr 34(5):1117–1134
Niwa Y, Hibiya T (2011) Estimation of baroclinic tide energy available for deep ocean mixing based on three-dimensional global numerical simulations. J Oceanogr 67(4):493–502. https://doi.org/10.1007/s10872-011-0052-1
Niwa Y, Hibiya T (2014) Generation of baroclinic tide energy in a global three-dimensional numerical model with different spatial grid resolutions. Ocean Model 80:59–73. https://doi.org/10.1016/j.ocemod.2014.05.003
Noh Y, Kim HJ (1999) Simulations of temperature and turbulence structure of the oceanic boundary layer with the improved near-surface process. J Geophys Res 104(C7):15621–15634
Oka A, Niwa Y (2013) Pacific deep circulation and ventilation controlled by tidal mixing away from the sea bottom. Nature Comm. https://doi.org/10.1038/ncomms3419
Osborn TR (1980) Estimates of the local rate of vertical diffusion from dissipation measurements. J Phys Oceanogr 10:83–89
Polzin KL (2009) An abyssal recipe. Ocean Model 30:298–309. https://doi.org/10.1016/j.ocemod.2009.07.006
Polzin KL, Toole JM, Ledwell JR, Schmitt RW (1997) Spatial variability of turbulent mixing in the abyssal ocean. Science 276:93–96
Prather MJ (1986) Numerical advection by conservation of second-order moments. J Geophys Res 91(D6):6671–6681
Roemmich D, Hautala S, Rudnick DL (1996) Northward abyssal transport through the Samoan passage and adjacent regions to diffusivities. J Geophys Res 101(C6):14039–14055
Röske F (2001) An atlas of surface fluxes based on the ECMWF Re-Analysis—a climatological dataset to force global ocean general circulation models. Max-Planck Institute for Meteorology Report 323
Rudnick DL (1997) Direct velocity measurements in the Samoan Passage. J Geophys Res 102(C2):3293–3302
Schmitz WJ (1995) On the interbasin-scale thermohaline circulation. Rev Geophysics 33(2):151–173
Simmons HL, Jayne SR, St. Laurent LC, Weaver AJ (2004) Tidally driven mixing in a numerical model of the ocean general circulation. Ocean Model 6:245–263. https://doi.org/10.1016/S1463-5003(03)00011-8
Sloyan BM, Wijffels SE, Tilbrook B, Katsumata K, Murata A, Macdonald AM (2013) Deep ocean changes near the western boundary of the South Pacific Ocean. J Phys Oceanogr 43:2132–2141. https://doi.org/10.1175/JPO-D-12-0182.1
St. Laurent LC, Schmitt RW (1999) The contribution of salt fingers to vertical mixing in the north Atlantic tracer release experiment. J Phys Oceanogr 29(6):1404–1424. https://doi.org/10.1175/1520-0485(1999)029%3c1404:TCOSFT%3e2.0.CO;2
St. Laurent LC, Toole JM, Schmitt RW (2001) Buoyancy forcing by turbulence above rough topography in the Abyssal Brazil Basin. J Phys Oceanogr 31:3476–3495
St. Laurent LC, Simmons HL, Jayne SR (2002) Estimating tidally driven mixing in the deep ocean. Geophys Res Lett 29(23):2106. https://doi.org/10.1029/2002GL015633
Steele M, Morley R, Ermold W (2001) PHC: a global ocean hydrography with a high-quality Arctic Ocean. J Climate 14(9):2079–2087. https://doi.org/10.1175/1520-0442(2001)014%3c2079:PAGOHW%3e2.0.CO;2
Talley LD (2013) Closure of the global overturning circulation through the Indian, Pacific, and Southern Oceans. Oceanogr 26(1):80–97. https://doi.org/10.5670/oceanog.2013.07
Tandon NF, Saenko GA, Cane MA, Kushner PJ (2020) Interannual variability of the global meridional overturning circulation dominated by Pacific Variability. J Phys Oceanogr 50:559–574. https://doi.org/10.1175/JPO-D-19-0129.1
Tatebe H, Ogura T, Nitta T, Komuro Y, Ogochi K, Takemura T, Sudo K, Sekiguchi M, Abe M, Saito F, Chikira M, Watanabe S, Mori M, Hirota N, Kawatani Y, Mochizuki T, Yoshimura K, Tanaka K, O'ishi R, Yamazaki D, Suzuki T, Kurogi M, Kataoka T, Watanabe M, Kimoto M (2019) Description and basic evaluation of simulated mean state, internal variability, and climate sensitivity in MIROC6. Geosci Model Dev. https://doi.org/10.5194/gmd-12-2727-2019
Urakawa LS, Hasumi H (2009) A remote effect of geothermal heat on the global thermohaline circulation. J Geophys Res 114:C07016. https://doi.org/10.1029/2008JC005192
Vic C, Garabato ACN, Green JAM, Waterhouse AF, Zhao Z, Melet A, de Lavergne C, Buijsman MC, Stephenson GR (2019) Deep-ocean mixing driven by small-scale internal tides. Nature Comm. https://doi.org/10.1038/s41467-019-10149-5
Voet G, Alford MH, Girton JB, Carter GS, Mickett JB, Klymak JM (2016) Warming and weakening of the abyssal flow through samoan passage. J Phys Oceanogr 46(8):2389–2401. https://doi.org/10.1175/JPO-D-16-0063.1
Voldoire A, Saint-Martin D, Sénési S, Decharme B, Alias A, Chevallier M, Colin J, Guérémy JF, Michou M, Moine MP, Nabat P, Roehrig R, Salas Mélia D, Séférian R, Valcke S, Beau I, Belamari S, Berthet S, Cassou C, Cattiaux J, Deshayes J, Douville H, Ethé C, Franchistéguy L, Geoffroy O, Lévy C, Madec G, Meurdesoif

Y, Msadek R, Ribes A, Sanchez-Gomez E, Terray L, Waldman R (2019) Evaluation of CMIP6 DECK experiments with CNRM-CM6-1. J Adv Model Earth Sys 11:2177–2213. https://doi.org/10.1029/2019MS001683

Waterhouse AF, Mackinnon JA, Nash JD, Alford MH, Kunze E, Simmons HL, Polzion KL, St. Laurent LC, Sun OM, Pinkel R, Talley LD, Whalen CB, Huussen TN, Carter GS, Fer I, Waterman S, Naveira Garabato AC, Sanford TB, Lee CM (2014) Global patterns of diapycnal mixing from measurements of the turbulent dissipation rate. J Phys Oceanogr 44(7):1854–1872. https://doi.org/10.1175/JPO-D-13-0104.1

Whalen CB, Mackinnon JA, Talley LD (2018) Large-scale impacts of the mesoscale environment on mixing from wind-driven internal waves. Nat Geosci 11:842–847. https://doi.org/10.1038/s41561-018-0213-6